RSC Advances

PAPER

View Article Online
View Journal | View Issue

Cite this: RSC Adv., 2017, 7, 55927

Enhanced photoreduction of Cr(VI) and photooxidation of NO over TiO_{2-x} mesoporous single crystals†

Yi Zhou,[a] Wenzhang Fang,[a] Yuanxin Deng,[a] Lihan Pan,[a] Bin Shen,[a] Hexing Li,[b] Yun Hu,[c] Haijun Chen,[d] Mingyang Xing*[a] and Jinlong Zhang*[a]

Managing air and water pollution is among the greatest challenges and a major issue for human civilizations in the 21st century. Semiconductors such as TiO_2 are regarded as one of the most promising catalysts that can be used to realize the simultaneous and efficient treatment of multi-component wastewater and NO selective oxidation. However, the granular TiO_2 always contains too many phase interfaces, which are harmful to the transfer of photo-excited electrons. Reduced TiO_2 mesoporous single crystals (TiO_{2-x} MSCs) with capacity of photoreduction and photooxidation were successfully synthesized by a facile hydrothermal treatment. The formation of Ti^{3+} impurity levels contribute to a narrowed band gap and enhanced visible light adsorption of TiO_{2-x}. In addition, the mesoporous single crystal structure would provide a long-range order channel for the transfer of photo-generated electrons, which leads to the efficient photoreduction and photooxidation capacity of TiO_{2-x} MSCs. The results revealed that Ti^{3+}-MSCs exhibit outstanding photocatalytic decontamination performance in simultaneous photodegradation of phenol and removal of Cr(VI) owing to high photo-generated charge separation rate and the synergistic effect of phenol and Cr(VI). In addition, in the absence of any noble metal, the as-prepared reduced Ti^{3+}-MSCs still show high selectivity of NO_2 in the NO_x photo-oxidation process, owing to the extended wide-spectrum absorption of Ti^{3+}-MSCs and the high-active holes on Ti^{3+}-MSCs under solar light irradiation.

Received 6th September 2017
Accepted 25th November 2017

DOI: 10.1039/c7ra09903g

rsc.li/rsc-advances

Open Access Article. Published on 11 December 2017. Downloaded on 2/14/2026 6:28:40 AM.
This article is licensed under a Creative Commons Attribution 3.0 Unported Licence.

Introduction

Photo-decontamination for the removal of toxic substances in wastewater from industrial processes such as leather tanning, electroplating and dyeing industries remains a huge challenge.[1] These toxic substances contain both organic and inorganic pollutants. The primary organic pollutants are aromatic hydrocarbons, such as phenols,[2,3] 1,4-dichlorobenzene,[4] tetracycline and rhodamine B[5] and the primary inorganic pollutants are heavy metals, such as Cr(VI),[6,7] Hg(II),[8] and Pd(II).[9] These pollutants pose a serious threat to human beings and other species because of their teratogenicity, carcinogenicity and biotoxicity.[10] The simultaneous removal of organic matter and toxic heavy metal ions from wastewater has particular significance to pollution control and decontamination.[11–15] Cr(VI) and phenol are two typical environmental contaminants that are widely used in industrial and military production.[16] The simultaneous reduction of hexavalent chromium (Cr(VI)) and oxidation of phenol has attracted plenty of attention.[17,18] In this respect, Cr(VI) could be photo-reduced to the less harmful Cr(III)[6,19] and phenol could be photo-oxidized into carbon dioxide or other eco-friendly organic matter by photocatalysts.[2,20] Moreover, because of the high oxidation capacity of Cr(VI), it can be easily reduced by reductants such as sodium bisulfite.[21] Nevertheless, a reductant dose larger than the stoichiometric amount has to be used for effective reduction. Adversely, secondary pollution is often caused. Alternatively, photocatalysts are regarded as an eco-friendly and efficient solution to this problem. To date, plenty of research has been reported on simultaneous removal of Cr(VI) and phenol by the TiO_2-based photocatalysis process. In our previous study,[3] mesoporous TiO_2 single crystals (MSCs) were considered as ideal photo-catalysts for simultaneous photo-decontamination of wastewater containing phenol and Cr(VI) owing to their perfect single crystalline structures, catalytically active facets and large surface areas. However, the

---

[a] *Key Laboratory for Advanced Materials, Institute of Fine Chemicals, School of Chemistry and Molecular Engineering, East China University of Science and Technology, 130 Meilong Road, Shanghai 200237, PR China. E-mail: mingyangxing@ecust.edu.cn; jlzhang@ecust.edu.cn*

[b] *Education Ministry Key Lab of Resource Chemistry, Shanghai Key Laboratory of Rare Earth Functional Materials, Department of Chemistry, Shanghai Normal University, Shanghai 200234, PR China*

[c] *School of Environment and Energy, South China University of Technology, Guangzhou 510006, PR China*

[d] *Department of Electronics and Tianjin Key Laboratory of Photo-Electronic Thin Film Device and Technology, Nankai University, Tianjin, 300071, China*

† Electronic supplementary information (ESI) available. See DOI: 10.1039/c7ra09903g

Open Access Article. Published on 11 December 2017. Downloaded on 2/14/2026 6:28:40 AM.
This article is licensed under a Creative Commons Attribution 3.0 Unported Licence.

photocatalytic activities of TiO_2 MSCs are limited by their relatively wide band gap (3.2 eV) and the high recombination rate of the photo-generated charges.[2,22,23]

Moreover, air pollution also poses a serious threat to the ecosystem. Nitric oxide (NO_x) pollutants are primarily responsible for acid precipitation, photo-chemical smog, and ozone depletion.[24] There two most common compounds of the nitric oxide group are NO[25] and NO_2.[26] The majority of nitric oxide emissions result from industrial furnaces, fossil fuel burning and internal combustion engines.[27] Therefore, the development of new methods to control NO_x emission has attracted much attention in recent years. However, these methods usually require high temperatures and specific equipment, which are not economical choices and could cause secondary pollution. Therefore, photocatalytic NO oxidation is regarded as an ideal method owing to its low-cost, facile reaction conditions and eco-friendliness. In general, there are three types of catalysts for NO oxidation: noble metal catalysts,[28,29] metal oxides catalysts[30] and ion-exchanged zeolites.[31] Hence, TiO_2 MSCs are regarded as promising photocatalysts for selective oxidation in the gas phase.

Herein, reduced TiO_2 mesoporous single crystals (Ti^{3+}-MSCs) with stable titanous doping were successfully synthesized by a facile hydrothermal treatment. They had a stable blue appearance because of the generation of Ti^{3+} and oxygen vacancies. The Ti^{3+} impurity level below the conduction band contributes to the narrowing of the band gap and extended absorption of solar light. By the *in situ* self-modification of MSCs, an outstanding photocatalytic decontamination performance for simultaneous photo-degradation of phenol and Cr(VI) can be achieved. Furthermore, new applications in environmental protection such as high activity and selectivity of NO_2 in NO_x photo-oxidation process can also be realized.

Experimental

Materials and methods

Preparation of TiO_{2-x} mesoporous single crystals (Ti^{3+}-MSCs). The TiO_{2-x} MSCs were prepared by the hard-template self-assembly method according to our previous report (details in the ESI†),[2] which exhibit a blue color appearance due to the generation of Ti^{3+} in the bulk of MSCs. Hence, the blue TiO_{2-x} MSCs were denoted as Ti^{3+}-MSCs. The TiO_2 mesoporous single crystals without Ti^{3+} doping were also prepared by the following procedure: 0.1 g Ti^{3+}-MSCs were calcined at 500 °C for 1 h in air with a heating rate of 2 °C min^{-1}. The obtained white products were denoted as MSCs.

Characterizations

The phase compositions of all catalysts were determined in air by powder X-ray diffraction measurements (XRD) using a Rigaku Ultima IV diffraction meter equipped with Cu Kα radiation ($\lambda = 1.5406$ Å). Data were collected while varying 2θ between 10 and 80°. The Raman spectra measurements were recorded with a Renishaw inVia Reflex Raman spectrometer with 524.5 nm laser excitation. The morphologies of all the composites were characterized by transmission electron microscopy (JEM-2100, JEOL) and field emission scanning electron microscopy (FESEM, Nova Nano-SEM 450). The electron paramagnetic resonance (EPR) spectra were recorded on a Bruker EMX 8/2.7 EPR spectrometer at an X-band frequency of 9.464 GHz, a sweep width of 1000.00 Gauss, and a center field of 3450.00 Gauss. The shift of the binding energy was referenced to the C1s level at 284.6 eV as an internal standard. The ultraviolet-visible (UV-vis) diffuse reflectance spectra (DRS) were measured on a SHIMADZU UV-2600 spectrometer equipped with an integrating sphere assembly and using $BaSO_4$ as the reference sample. The photoluminescence (PL) emission spectra of the solid catalysts were also recorded at room temperature (25 °C) using luminescence spectrometry (Cary Eclipse) under the excitation light at 310 nm. All the electrochemical experiments were carried out at room temperature in a cell with a standard three-electrode system using an electrochemical analyzer (CHI 660 D electrochemical station, CHI Instruments Inc.). The electrode system consisted of a working electrode (as-prepared samples as the working electrodes with an active area of *ca.* 0.5 cm^{-2}), a Pt wire as the counter electrode and a saturated Ag/AgCl as the reference electrode. Transient photocurrent responses of different samples were studied in 0.5 M Na_2SO_4 aqueous solution under various irradiation conditions (300 W Xe lamp).

Photoreduction and photooxidation tests

Synchronous removal of phenol and Cr(VI). Phenol and potassium bichromate (phenol & $K_2Cr_2O_7$, 20 mg L^{-1}) (as simulative pollutants) were degraded to evaluate the photocatalytic activity of each sample. Initially, 50 mg photocatalyst was added into a 100 mL quartz photocatalytic reactor, followed by the addition of 50 mL phenol & $K_2Cr_2O_7$ solution; then, the pH value was fixed at 4.0 by HCl (0.1 M) adjustment. The mixture was stirred for 30 min in the absence of light to achieve the adsorption–desorption equilibrium. The solar light source was provided by a 300 W He lamp with AM 1.5 filters. The intensity of light was 100 mW cm^{-2}, measured with a UVA radiometer, and the intensity of light was ensured to be consistent for each test. The concentration of Cr(VI) was measured spectrophotometrically using the DPC (diphenylcarbazide) method with some modifications. Initially, 200 μL of the prepared DPC reagent (50 mL of D.I. water and 50 mL of the DPC reagent that contains 50 mL of acetone and 0.2 g of DPC) was added to an acidulated sample solution (20 μL mixture of H_2SO_4 and water volume ratio of 1 : 1, 20 μL mixture of H_3PO_4 and water volume ratio of 1 : 1 and 3.5 mL sample solution). The solution was blended well and kept standing for 15 min before the analysis. The absorbance measurements at 540 nm were performed using a UV-vis spectrophotometer (SHIMADZU UV-2600).

Photooxidation of NO. The NO_x photo-oxidation activities of samples were investigated at room temperature in a continuous flow reactor. The experimental setup was described in a previous report.[32] Briefly, 20 mg catalyst was spread out at the bottom of the reactor. The feed gas contained 40 ± 1 ppm NO

This journal is © The Royal Society of Chemistry 2017

Open Access Article. Published on 11 December 2017. Downloaded on 2/14/2026 6:28:40 AM.
This article is licensed under a Creative Commons Attribution 3.0 Unported Licence.

with humidity of 70%, and the flow rate was maintained at 200 mL min^{-1}. The feed gas was obtained by diluting NO with a high concentration of 1000 ppm with N_2 and by bubbling in water with air stream. A 500 W commercial tungsten halogen lamp (General Electric) with a glass filter that cut off the light below 420 nm was used as the visible light source. The light intensity was 0.7 mW cm^{-2}, measured with a UVA radiometer (Photoelectric Instrument Factory of Beijing Normal University). Before light irradiation, the catalysts were treated with the feed gas stream for 10 min in the absence of light to achieve the adsorption–desorption equilibrium. The light simply shuttered for each test, so the intensity of light was ensured to be consistent. Reference experiments were tested and the results indicated that NO could not be converted when the reactor was irradiated in the absence of any samples or in the presence of the catalyst without light source. For data analysis, the NO conversion, the NO removal, the yield of NO_2 and the total NO_x removal were defined as follows:

$$\text{NO conversion }(\%) = \frac{\text{NO}_{\text{in}} - \text{NO}_{\text{out}}}{\text{NO}_{\text{in}}} \times 100\%$$

$$\text{NO removal }\left(\mu\text{mol g}^{-1}\right) = 20 \times \int \frac{f}{22.4}(\text{NO}_{\text{in}} - \text{NO}_{\text{out}})\text{d}t$$

$$\text{Yield of NO}_2\ \left(\mu\text{mol g}^{-1}\right) = 20 \times \int \frac{f}{22.4}(\text{NO}_{2\ \text{out}} - \text{NO}_{2\ \text{in}})\text{d}t$$

$$\text{Total NO}_x\text{ removal }(\mu\text{mol g}^{-1}) = \text{NO removal} - \text{yield of NO}_2$$

(f shows the quantity of reaction air flow under standard state).

Results and discussion

The TEM and FESEM images of Ti^{3+}-MSCs are shown in Fig. 1a and b, respectively. The images show that the obtained Ti^{3+}-MSCs exhibit a tetragonal bipyramid profile and an ordered mesoporous structure with a size of 700–800 nm, which is consistent with the result of the low-magnified FESEM (Fig. S1†). The pore size of the Ti^{3+}-MSCs is about 45 nm. The type IV N_2 sorption isotherm curves and the Barrett–Joyner–Halenda pore size distribution centered at 40–50 nm confirm the mesoporous nature of the structure (Fig. S2†). The magnified image of Ti^{3+}-MSCs is shown in Fig. 1c. It indicates that the edges of Ti^{3+}-MSCs are relatively smooth. The corresponding selected area electron diffraction (SAED) patterns in the insets of Fig. 1c confirm that Ti^{3+}-MSCs are single crystal structured.[33] The diffraction lattice matrix of (110) is parallel to the {110} facets and vertical to the diffraction lattice matrix of (001), which indicates that TiO_2 prefers to form a [001]-oriented tetragonal rutile single crystal with dominant {110} facets owing to the influence of HCl in lowering the activation energy for the rutile formation. The (101) facets can be observed in HRTEM (Fig. 1d). All the lattice fringes have long-term orderly arrangements, indicating the single crystalline nature of Ti^{3+}-MSCs, which implies the capacities of MSCs for high electron mobility.

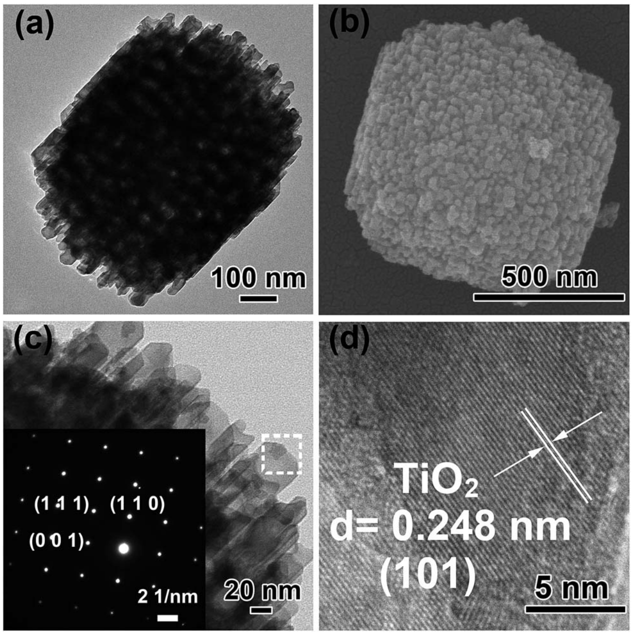

Fig. 1 (a) TEM image of Ti^{3+}-MSCs, (b) FESEM image of Ti^{3+}-MSCs, (c) and (d) HRTEM image of Ti^{3+}-MSCs. Insets of (c) shows the corresponding SAED pattern of Ti^{3+}-MSCs.

The crystalline structures of Ti^{3+}-MSCs and MSCs were investigated by XRD. As shown in Fig. 2a, the XRD patterns of Ti^{3+}-MSCs and MSCs show almost the same peaks, which can be indexed to the characteristic diffraction peaks of rutile TiO_2 (JCPDS 12-1276). In addition, Ti^{3+}-MSCs and MSCs exhibit strong diffraction peaks, indicating that the obtained catalysts have high crystallinity. The blue Ti^{3+}-MSCs were calcinated in air to obtain the white MSCs. Compared with that of MSCs, the absorption shoulder of Ti^{3+}-MSCs shows a significant red-shift (Fig. 2b). The absorption intensity in the range of 400–700 nm of Ti^{3+}-MSCs clearly increases with titanous doping. The color of Ti^{3+}-MSCs was blue, while MSCs turned to be white. This could be attributed to the generation of Ti^{3+} and oxygen vacancies in the bulk or on the surface of the Ti^{3+}-MSCs.[34,35] This result is consistent with other studies that have been reported previously.[36] Moreover, the bandgap of Ti^{3+}-MSCs also has a distinct decrease from 3.09 eV to 3.01 eV compared with that of MSCs, implying that the formation of the Ti^{3+} impurity level contributes to the narrowing of the bandgap of Ti^{3+}-MSCs.

In order to investigate the reason of the enhancement of visible light absorption over Ti^{3+}-MSCs, we performed EPR test on each sample (Fig. 3a). MSCs show no Ti^{3+} signals in the EPR spectra owing to the oxidation of Ti^{3+} during the calcination process. The EPR signals of Ti^{3+}-MSCs with $g_{\perp} = 1.966$ and $g_{\parallel} = 1.939$ were observed, which should be ascribed to the Ti^{3+} species in the bulk of TiO_2.[37,38] The strong Ti^{3+} signals of Ti^{3+}-MSCs in low temperature EPR imply high concentration of Ti^{3+} in the catalyst.[39,40] Moreover, because the EPR signals and the g-value of rutile are different from those of the anatase, the results confirm the rutile phase of the as-prepared sample.[41] Moreover,

Open Access Article. Published on 11 December 2017. Downloaded on 2/14/2026 6:28:40 AM.
This article is licensed under a Creative Commons Attribution 3.0 Unported Licence.

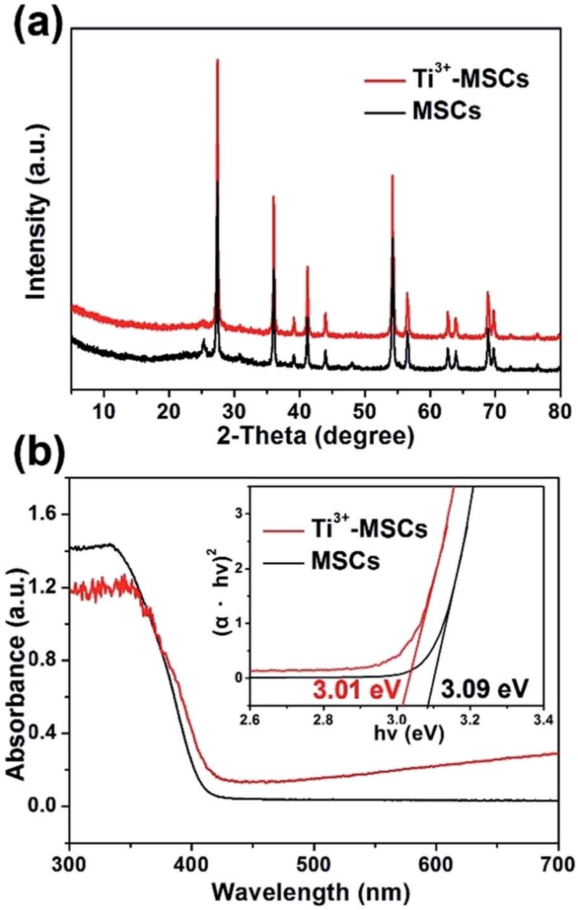

Fig. 2 (a) XRD spectra of MSCs and Ti^{3+}- MSCs, and (b) UV-vis DRS spectra and transformed Kubelka–Munk function against the photon energy plot (inset) of MSCs and Ti^{3+}-MSCs.

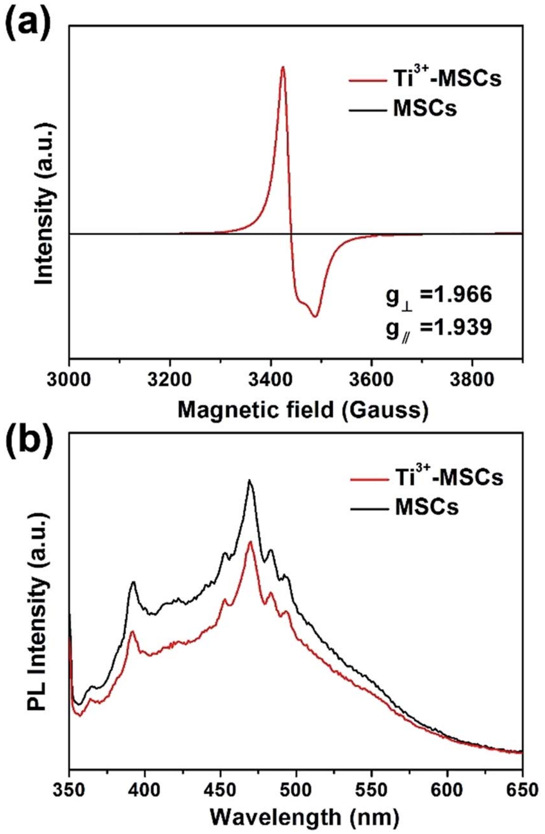

Fig. 3 (a) EPR spectra of MSCs and Ti^{3+}-MSCs on 77 K, and (b) PL spectra of MSCs and Ti^{3+}-MSCs.

photoluminescence (PL) emission spectra analysis was used to better understand the transfer and recombination process of photogeneration charges in the semiconductor photocatalyst (Fig. 3b). The intensity of PL increases immediately after calcination, so MSCs have a higher PL signal than Ti^{3+}-MSC. Compared with the MSCs, the Ti^{3+} doping catalysts exhibit lower PL intensity of around 370 nm and 475 nm, indicating low recombination rate of the photo-generated electron–hole pairs, and higher photoactivity. It is reasonable to ascribe the lower recombination of electrons and holes to the capture of holes by surface oxygen vacancy and defects.[42,43] Therefore, more electrons would remain and participate in the photoreduction process, which predicates a higher photoreduction activity of Ti^{3+}-MSCs. The trapping holes in oxygen vacancies act as an active site for the photo-oxidation process.

The simultaneous photo-degradation of phenol and removal of Cr(VI) under solar light illumination were evaluated to analyze the synergistic photocatalytic decontamination between phenol and Cr(VI) (Fig. 4). According to the previous report,[44] the Cr(VI) reduction efficiencies were good at $pH \leq 4$, particularly showing highest reduction efficiencies at $pH = 2.3$. In the synchronous removal of phenol and Cr(VI) test, however, we employed UV-vis spectrophotometry and HPLC to measure the concentration of Cr(VI) and phenol over one solution at the same time, respectively. A low pH value shows some disadvantages of the HPLC test for phenol. Hence, the suitable pH value for the photocatalytic removal of Cr(VI) in our study was recommended as 4.0. In addition, the chromium ions ($Cr_2O_7^{2-}$) of $H_2Cr_2O_7$ resulted in low pH values and the photo-removal process of Cr(VI) took place as shown in eqn (1):[44]

$$Cr_2O_7^{2-} + 14H^+ + 6e^- \rightarrow 2Cr(\text{III}) + 7H_2O \tag{1}$$

As shown in the equation above, the existence of abundant H^+ is advantageous to the photocatalytic removal of Cr(VI). Fig. 4a demonstrates the photocatalytic reduction of Cr(VI) over a variety of as-prepared catalysts at $pH = 4.0$. Ti^{3+}-MSCs show much higher photo-reduction activity than MSCs. The photo-reduction rate of Cr(VI) over Ti^{3+}-MSCs without phenol was slower than that with phenol. The existence of phenol could enhance the removal of Cr(VI) by acting as the scavenger of photo-generated holes. Moreover, an electron or hole trapping agent was added into the reaction solution to investigate synergistic photocatalytic decontamination between phenol and Cr(VI) processes. Upon addition of the electron trapping agent (sodium iodate, $NaIO_3$) to the solution containing Ti^{3+}-MSCs, the photo-reduction activity of Cr(VI) for Ti^{3+}-MSCs significantly decreases, indicating that irradiated Ti^{3+}-MSCs have higher active electron concentration. Nevertheless, the

Open Access Article. Published on 11 December 2017. Downloaded on 2/14/2026 6:28:40 AM.
This article is licensed under a Creative Commons Attribution 3.0 Unported Licence.

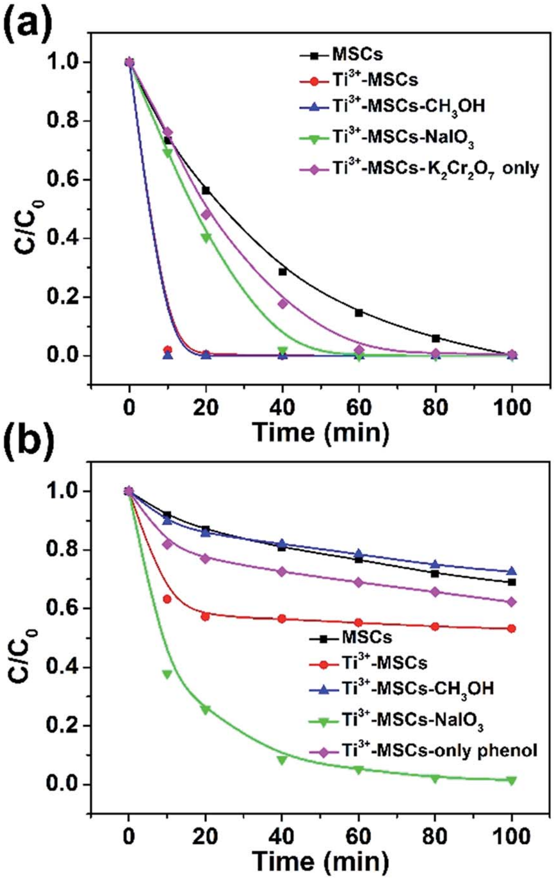

Fig. 4 The synchronous photocatalytic degradation dynamics of (a) Cr(VI) and (b) phenol over different catalysts under simulated solar light irradiation (with an AM 1.5 air mass filter).

removal activity of Cr(VI) for the Ti^{3+} doped sample has no significant change when the hole trapping agent (methanol, CH_3OH) was injected, indicating the electrons would directly involve in the Cr(VI) reduction reaction. For photo-oxidation of phenol (Fig. 4b), Ti^{3+}-MSCs exhibit higher activity than MSCs. The photodegradation rate of phenol over Ti^{3+}-MSCs without Cr(VI) was slower than that with Cr(VI). This indicated that the existence of Cr(VI) could promote the degradation of phenol by acting as a sacrificial agent of holes. Upon addition of CH_3OH, however, the oxidation rate of phenol for Ti^{3+}-MSCs reduces sharply, indicating that irradiated Ti^{3+}-MSCs generate more holes in the phenol-oxidation process. In addition, the electron trapping agent, $NaIO_3$, shows remarkable promotion effect in the photo-degradation process of phenol, indicating that the holes were not directly involved in the phenol oxidation. The holes were reacted with H_2O molecules to generate the hydroxyl radicals, which are responsible for the photooxidation of phenol. The addition of $NaIO_3$ would trap the electrons and prolong the lifetime of holes to produce abundant hydroxyl radicals. Interestingly, when the concentration of Cr(VI) reduced to nearly zero, the photo-oxidation rate of phenol decreased sharply (red line fixed at 10 min and green line fixed at 40 min, as shown in Fig. 4a and b), indicating that the presence of Cr(VI) promoted the oxidation rate of phenol.[44] This result is ascribed to the synergistic effect between the photo-oxidation of phenol and the photo-reduction of Cr(VI).[9]

Photooxidation of NO gas under solar light was used to evaluate the gas photocatalytic activities of the as-prepared Ti^{3+}-MSCs (Fig. 5). The light was turned on after NO adsorption–desorption equilibrium was achieved. Since the light was turned on, the concentration of NO decreased sharply and the concentration of NO_2 simultaneously increased (Fig. 5a). However, the increase in NO_2 concentration is very slow. The chemisorption of NO caused by photogenerated hydroxyl radicals leads to the plunge in the concentration of NO.[45] It is worth noting that the concentration of NO does not reduce, which indicates that the adsorption saturation has been reached. Then, the concentration of NO_2 increases with the illumination time. After 10 min of light irradiation, the gas concentrations varied slowly. Moreover, all nitrogen in the gas phase approximately achieves equilibrium after 60 min of irradiation as shown in eqn (2).

$$NO_{out}\,(37.0\text{ ppm}) + NO_{2\,out}\,(4.0\text{ ppm}) \approx NO\text{ in }(41\text{ ppm}) \quad (2)$$

MSCs and Ti^{3+}-MSCs were evaluated for photo-decontamination of NO_x experiments to illustrate that the Ti^{3+}

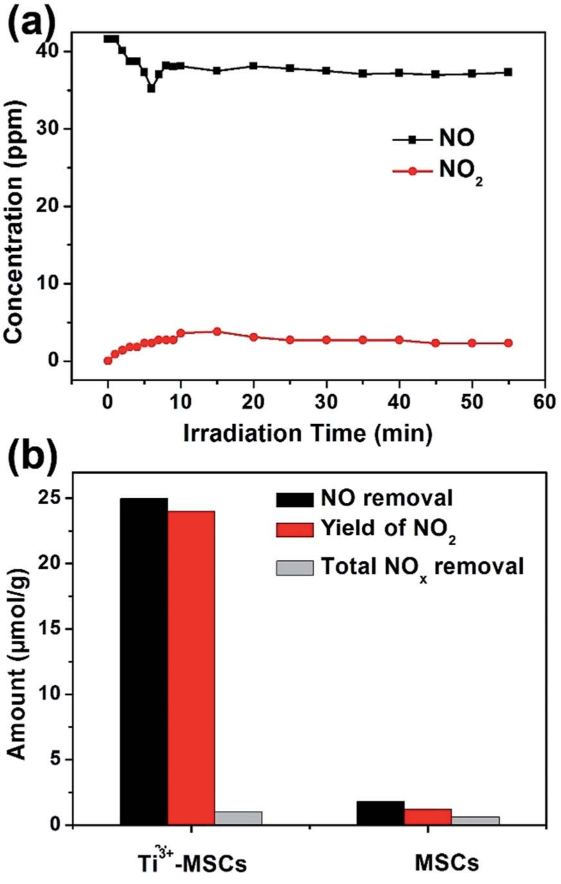

Fig. 5 (a) Time-course of the changes in concentration of NO, NO_2 in the presence of Ti^{3+}-MSCs under solar light irradiation, and (b) photocatalytic activity of MSCs and Ti^{3+}-MSCs under irradiation of solar light for 60 min.

Open Access Article. Published on 11 December 2017. Downloaded on 2/14/2026 6:28:40 AM.
This article is licensed under a Creative Commons Attribution 3.0 Unported Licence.

doping benefits the oxidation of NO_x (Fig. 5b). The NO removal amount within 60 min over Ti^{3+}-MSCs is 10 times as high as that over MSCs. Moreover, the yield of NO_2 within one hour over Ti^{3+}-MSCs is about 9 times higher than that over MSCs. The higher the percentage of NO transformed to NO_2, the lower is total NO_x removal. In other words, the selectivity of NO_2 is high over Ti^{3+}-MSCs. This could be attributed to the high separation rate of the photo-generated electrons and holes from irradiated Ti^{3+}-MSCs. In other words, the active holes sites efficiently promote the oxidation of NO.

In order to investigate the mechanism of photoreduction and photooxidation over Ti^{3+}-MSCs, the photoelectrochemical properties of these samples were also measured by transient photocurrent test under solar light irradiation as shown in Fig. 6a. The rise and fall of the photocurrent corresponded to the switching on and off of irradiation. Both samples show stable current intensity. However, the transient photocurrent of Ti^{3+}-MSCs is 1.5 times higher than that of MSCs. This result reveals the enhanced light absorption properties of Ti^{3+}-MSCs, which attribute to the higher separation rate of electrons and holes of Ti^{3+}-MSCs and its remarkable charge transfer ability owing to its long-range order crystallinity.[34,46] In addition, to validate our postulate that improved separation rate of photo-generated charges contributes to a better performance, we compared the electrochemical impedance spectra (EIS) of Ti^{3+}-MSCs and MSCs in dark. The semicircle in the Nyquist plots of Ti^{3+}-MSCs is significantly smaller than that of MSCs (Fig. 6b). In other words, the impedance of Ti^{3+}-MSCs is distinctly smaller than that of MSCs, suggesting a higher separation rate of electrons and holes and an excellent charge transfer process. This result is associated directly with a more efficient charge transfer process and better photoreduction and photooxidation activity over Ti^{3+}-MSCs.[47]

The proposed mechanism of synergistic photocatalytic decontamination between phenol and Cr(VI) on Ti^{3+}-MSCs is illustrated in Fig. 7. After Ti^{3+} doping, the generation of abundant Ti^{3+} leads to the formation of the Ti^{3+} impurity level under the conduction band (CB) of the mesoporous titanium dioxide single crystal, which contributes to a narrowed band gap and also an extended solar light absorption of TiO_2-MSCs to the visible light region. Ti^{3+}-MSCs efficiently utilize the visible light in the photo-redox reaction. In addition, TiO_{2-x} mesoporous single crystals are excited by solar light to generate electrons and holes, and some of the holes are captured by the oxygen vacancy (top of Fig. 7). This leads to high separation efficiency of electrons and holes, and the longer lifetime of electrons. This can be confirmed by the results of photoluminescence (PL) emission spectra analysis. Subsequently, electrons can directly participate in the reduction of Cr(VI). Therefore, in our designed system, Ti^{3+}-MSCs exhibit an excellent performance in simultaneous photodegradation of phenol and removal of Cr(VI) in liquid state reaction, owing to the synergistic effect of Cr(VI) and phenol. Furthermore, for Ti^{3+}-MSCs, as more active holes are

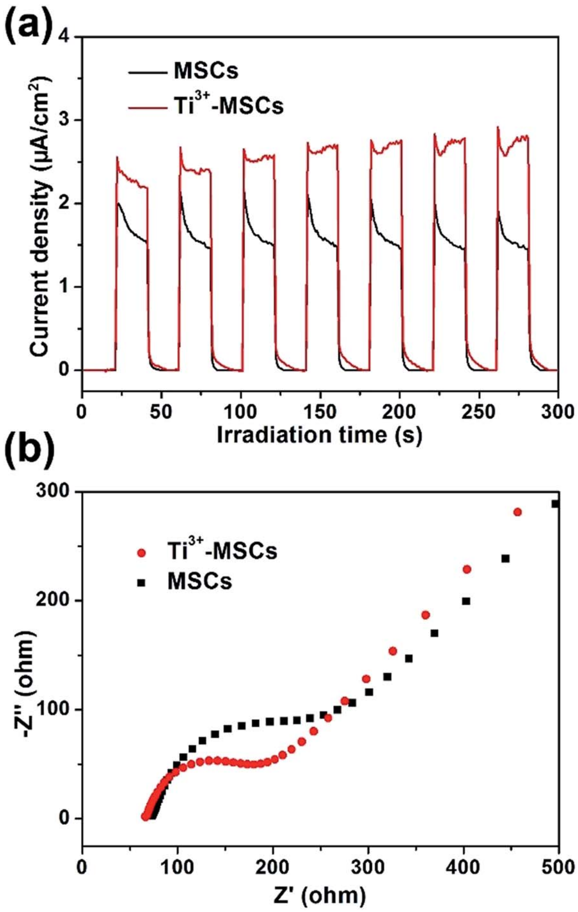

Fig. 6 (a) Transient photocurrent responses of MSCs and Ti^{3+}-MSCs (300 W Xe lamp with AM 1.5 filter), and (b) EIS changes of MSCs and Ti^{3+}-MSCs in dark (the EIS measurements were performed in the presence of a 2.0 mM $K_3[Fe(CN)_6]$ and 0.5 M KCl mixture aqueous solution).

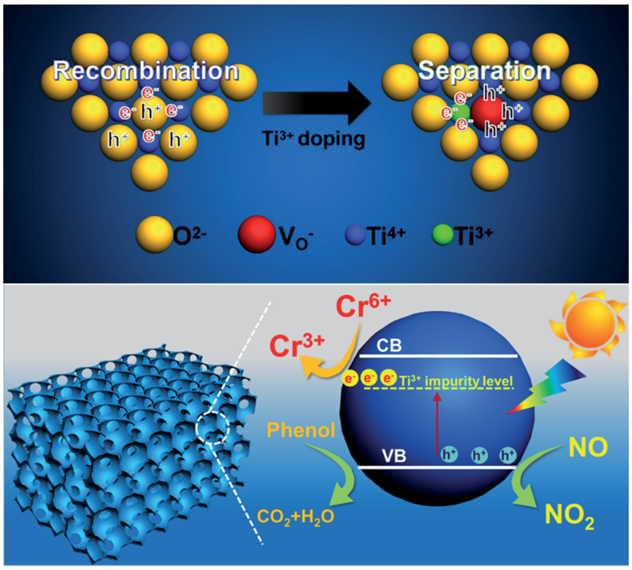

Fig. 7 Schematic diagram of photogenerated charges distribution (top) and the proposed mechanism for photo-reduction of Cr(VI) and photo-oxidation of phenol or NO_x over Ti^{3+}-MSCs under solar light irradiation (bottom).

Open Access Article. Published on 11 December 2017. Downloaded on 2/14/2026 6:28:40 AM. This article is licensed under a Creative Commons Attribution 3.0 Unported Licence.

involved in the oxidation of NO, higher activity is obtained owing to its low recombination rate of electrons and holes.

Conclusions

A blue reduced titanium dioxide mesoporous single crystal with Ti^{3+} doping was synthesized using a simple hydrothermal method. According to the results of the EPR measurements, the amount of Ti^{3+} species of Ti^{3+}-MSCs is higher than MSCs. The self-doping of Ti^{3+} contributes to the formation of impurity levels just below the conduction band, which results in the narrowing of the band gap. Moreover, the oxygen vacancies in Ti^{3+}-MSCs lead to a high photo-generated charge separation rate and prolonged lifetime of the electrons. Hence, the obtained Ti^{3+}-MSCs present an extended wide-spectrum light absorption in the range of 400–700 nm and high capacities for electron mobility. The obtained metal-free Ti^{3+}-MSCs exhibit outstanding photocatalytic decontamination performance in simultaneous removal of phenol and Cr(VI). The active electrons of Ti^{3+}-MSCs, high photo-generated charges separation rate and synergistic effect between phenol and Cr(VI) lead to these high decontamination abilities. Furthermore, high-concentrated oxygen vacancies of Ti^{3+}-self doped MSCs lead to an improved selectivity of NO_2 in the NO_x photo-oxidation process.

Conflicts of interest

The authors declare no competing financial interest.

Acknowledgements

This work was supported by the National Natural Science Foundation of China (21577036, 21377038, 21237003, 21677048), State Key Research Development Program of China (2016YFA0204200), the "Chenguang Program" from Shanghai Education Development Foundation and Shanghai Municipal Education Commission (14CG30), Science and Technology Commission of Shanghai Municipality (16JC1401400, 17520711500), Shanghai Pujiang Program (17PJD011), and the Fundamental Research Funds for the Central Universities (22A201514021).

References

1 R. Qiu, D. Zhang, Z. Diao, X. Huang, C. He, J.-L. Morel and Y. Xiong, *Water Res.*, 2012, **46**, 2299–2306.
2 Y. Zhou, Q. Yi, M. Xing, L. Shang, T. Zhang and J. Zhang, *Chem. Commun.*, 2016, **52**, 1689–1692.
3 T. Wang, Z.-y. Xu, L.-g. Wu, B.-r. Li, M.-x. Chen, S.-y. Xue, Y.-c. Zhu and J. Cai, *RSC Adv.*, 2017, **7**, 31921–31929.
4 Y. Tae Kwon, K. Yong Song, W. In Lee, G. Jin Choi and Y. Rag Do, *J. Catal.*, 2000, **191**, 192–199.
5 L. Zhou, L. Wang, J. Zhang, J. Lei and Y. Liu, *Res. Chem. Intermed.*, 2017, **43**, 2081–2101.
6 D. Lu, W. Chai, M. Yang, P. Fang, W. Wu, B. Zhao, R. Xiong and H. Wang, *Appl. Catal., B*, 2016, **190**, 44–65.
7 Y. Yang, G. Wang, Q. Deng, H. Wang, Y. Zhang, D. H. L. Ng and H. Zhao, *RSC Adv.*, 2014, **4**, 34577–34583.
8 G. Chi, B. Shen, R. Yu, C. He and X. Zhang, *J. Hazard. Mater.*, 2017, **330**, 83–92.
9 D. Lu, M. Yang, P. Fang, C. Li and L. Jiang, *Appl. Surf. Sci.*, 2017, **399**, 167–184.
10 H. Qin, Y. Bian, Y. Zhang, L. Liu and Z. Bian, *Chin. J. Chem.*, 2017, **35**, 203–208.
11 Y. Choi, M. S. Koo, A. D. Bokare, D.-h. Kim, D. W. Bahnemann and W. Choi, *Environ. Sci. Technol.*, 2017, **51**, 3973–3981.
12 L. Wang, N. Wang, L. Zhu, H. Yu and H. Tang, *J. Hazard. Mater.*, 2008, **152**, 93–99.
13 S. Dong, J. Feng, M. Fan, Y. Pi, L. Hu, X. Han, M. Liu, J. Sun and J. Sun, *RSC Adv.*, 2015, **5**, 14610–14630.
14 P. K. Boruah, P. Borthakur, G. Darabdhara, C. K. Kamaja, I. Karbhal, M. V. Shelke, P. Phukan, D. Saikia and M. R. Das, *RSC Adv.*, 2016, **6**, 11049–11063.
15 K. Kabra, R. Chaudhary and R. L. Sawhney, *Ind. Eng. Chem. Res.*, 2004, **43**, 7683–7696.
16 R. Vinu and G. Madras, *Environ. Sci. Technol.*, 2008, **42**, 913–919.
17 H.-M. Zhang, W. Xu, Z. Fan, X. Liu, Z.-C. Wu and M.-H. Zhou, *Sep. Purif. Technol.*, 2017, **172**, 152–157.
18 O. M. Ontañon, P. S. González, G. G. Barros and E. Agostini, *New Biotechnol.*, 2017, **37**, 172–179.
19 H. Chen, Y. Shao, Z. Xu, H. Wan, Y. Wan, S. Zheng and D. Zhu, *Appl. Catal., B*, 2011, **105**, 255–262.
20 V. Makrigianni, A. Giannakas, C. Daikopoulos, Y. Deligiannakis and I. Konstantinou, *Appl. Catal., B*, 2015, **174**, 244–252.
21 G. Qin, M. J. McGuire, N. K. Blute, C. Seidel and L. Fong, *Environ. Sci. Technol.*, 2005, **39**, 6321–6327.
22 Y. Zhang, Z.-R. Tang, X. Fu and Y.-J. Xu, *ACS Nano*, 2010, **4**, 7303–7314.
23 C. Dong, H. Song, Y. Zhou, C. Dong, B. Shen, H. Yang, M. Matsuoka, M. Xing and J. Zhang, *RSC Adv.*, 2016, **6**, 77863–77869.
24 N. Tang, Y. Liu, H. Wang and Z. Wu, *J. Phys. Chem. C*, 2011, **115**, 8214–8220.
25 M. Ghafari and J. D. Atkinson, *Environ. Sci. Technol.*, 2016, **50**, 5189–5196.
26 I. Papailias, N. Todorova, T. Giannakopoulou, J. Yu, D. Dimotikali and C. Trapalis, *Catal. Today*, 2017, **280**, 37–44.
27 K. Skalska, J. S. Miller and S. Ledakowicz, *Sci. Total Environ.*, 2010, **408**, 3976–3989.
28 D. Bhatia, R. W. McCabe, M. P. Harold and V. Balakotaiah, *J. Catal.*, 2009, **266**, 106–119.
29 J. Jelic, K. Reuter and R. Meyer, *ChemCatChem*, 2010, **2**, 658–660.
30 J. Giménez-Mañogil, A. Bueno-López and A. García-García, *Appl. Catal., B*, 2014, **152**, 99–107.
31 M. Iwamoto, H. Furukawa, Y. Mine, F. Uemura, S.-i. Mikuriya and S. Kagawa, *J. Chem. Soc., Chem. Commun.*, 1986, 1272–1273, DOI: 10.1039/C39860001272.
32 Y. Hu, X. Song, S. Jiang and C. Wei, *Chem. Eng. J.*, 2015, **274**, 102–112.

Open Access Article. Published on 11 December 2017. Downloaded on 2/14/2026 6:28:40 AM. This article is licensed under a Creative Commons Attribution 3.0 Unported Licence.

33 H. G. Yang, C. H. Sun, S. Z. Qiao, J. Zou, G. Liu, S. C. Smith, H. M. Cheng and G. Q. Lu, *Nature*, 2008, **453**, 638–641.

34 W. Fang, L. Khrouz, Y. Zhou, B. Shen, C. Dong, M. Xing, S. Mishra, S. Daniele and J. Zhang, *Phys. Chem. Chem. Phys.*, 2017, **19**, 13875–13881.

35 Y. Zhou, Y. Liu, P. Liu, W. Zhang, M. Xing and J. Zhang, *Appl. Catal., B*, 2015, **170–171**, 66–73.

36 F. Zuo, L. Wang, T. Wu, Z. Zhang, D. Borchardt and P. Feng, *J. Am. Chem. Soc.*, 2010, **132**, 11856–11857.

37 L. Bonneviot and G. L. Haller, *J. Catal.*, 1988, **113**, 96–105.

38 W. Fang, M. Xing and J. Zhang, *J. Photochem. Photobiol., C*, 2017, **32**, 21–39.

39 W. Fang, Y. Zhou, C. Dong, M. Xing and J. Zhang, *Catal. Today*, 2016, **266**, 188–196.

40 W. Fang, M. Xing and J. Zhang, *Appl. Catal., B*, 2014, **160–161**, 240–246.

41 M. Liu, X. Qiu, M. Miyauchi and K. Hashimoto, *Chem. Mater.*, 2011, **23**, 5282–5286.

42 J. Yu, J. Fan and B. Cheng, *J. Power Sources*, 2011, **196**, 7891–7898.

43 J. Su, X. Zou and J.-S. Chen, *RSC Adv.*, 2014, **4**, 13979–13988.

44 F. Liu, J. Yu, G. Tu, L. Qu, J. Xiao, Y. Liu, L. Wang, J. Lei and J. Zhang, *Appl. Catal., B*, 2017, **201**, 1–11.

45 G. Guo, Y. Hu, S. Jiang and C. Wei, *J. Hazard. Mater.*, 2012, **223**, 39–45.

46 Z. Bian, T. Tachikawa and T. Majima, *J. Phys. Chem. Lett.*, 2012, **3**, 1422–1427.

47 C. Mao, F. Zuo, Y. Hou, X. Bu and P. Feng, *Angew. Chem., Int. Ed.*, 2014, **53**, 10485–10489.

This journal is © The Royal Society of Chemistry 2017